Template-Free Electrochemical Synthesis of Sn Nanofibers as High-Performance Anode Materials for Na-Ion Batteries

Do-Hwan Nam,* Tae-Hee Kim, Kyung-Sik Hong, and Hyuk-Sang Kwon*

Department of Materials Science and Engineering, Korea Advanced Institute of Science and Technology, 291 Daehak-ro, Yuseong-gu, Daejeon 305-701, Republic of Korea

ABSTRACT Sn nanofibers with a high aspect ratio are successfully synthesized using a simple electrodeposition process from an aqueous solution without the use of templates. The synthetic approach involves the rapid electrochemical deposition of Sn accompanied by the strong adsorption of Triton X-100, which can function as a growth modifier for the Sn crystallites. Triton X-100 is adsorbed on the {200} crystallographic planes of Sn in an elongated configuration and suppressed the preferential growth of Sn along the [100] direction. Consequently, the Sn electrodeposits are forced to grow anisotropically in a direction normal to the (112) or ($\bar{1}$12) plane, forming one-dimensional nanofibers. As electrode materials for the Na-ion batteries, the Sn nanofibers exhibit a high reversible capacity and an excellent cycle performance; the charge capacity is maintained at 776.26 mAh g^{-1} after 100 cycles, which corresponds to a retention of 95.09% of the initial charge capacity. The superior electrochemical performance of the Sn nanofibers is mainly attributed to the high mechanical stability of the nanofibers, which originate from highly anisotropic expansion during sodiation and the pore volumes existing between the nanofibers.

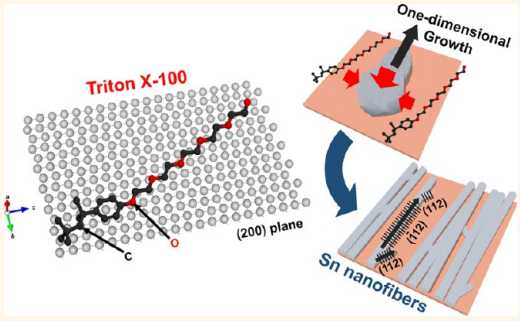

KEYWORDS: tin · nanofiber · electrodeposition · Na-ion battery · anode

In the past few decades, one-dimensional (1D) nanostructures, such as nanowires, nanorods, nanobelts and nanotubes, have received growing attention due to their highly desirable and fascinating properties.[1−4] Compared with the bulky counterparts, 1D nanostructures have distinct chemical and electrical properties and greater chemical reactivity. The properties originate from their unique geometric characteristics, including the ultrafine size effects, the long-range orientation of the crystalline lattice and the quantum confinement effects.[5−8] Accordingly, 1D nanostructures are expected to play important roles in nanotechnology and materials science. Driven by these factors, current research activities are mainly focused on the synthesis of metal nanostructures, for example, Sn-based nanowires and nanotubes, for a wide range of applications from electronic and photoelectronic devices[9,10] to chemical sensors[11,12] and electrode materials for Li-ion batteries.[13,14]

In general, there are two approaches for synthesizing 1D nanostructures, template-assisted synthesis and template-free synthesis. Template-assisted synthesis is one of the most effective methods for fabricating 1D nanostructures for diverse materials.[15−19] Through numerous synthetic methods, such as electrochemical deposition, sol−gel processing and chemical vapor deposition, the target materials grow in the free space of the template to form 1D morphologies.[15−19] Commonly, hard porous templates, such as anodic aluminum oxide (AAO) membranes[15,16] and porous polycarbonate membranes (PCM),[7,17−19] are used for the preparation of metal nanowires. It is generally accepted that template-assisted synthesis provides high-throughput and cost-effective procedures for fabricating well-defined 1D nanostructures. Nevertheless, this approach suffers from limitations when used to fabricate high-aspect-ratio 1D nanostructures because

* Address correspondence to dhnam@kaist.ac.kr, hskwon@kaist.ac.kr.

Received for review September 29, 2014 and accepted October 28, 2014.

Published online October 28, 2014
10.1021/nn505536t

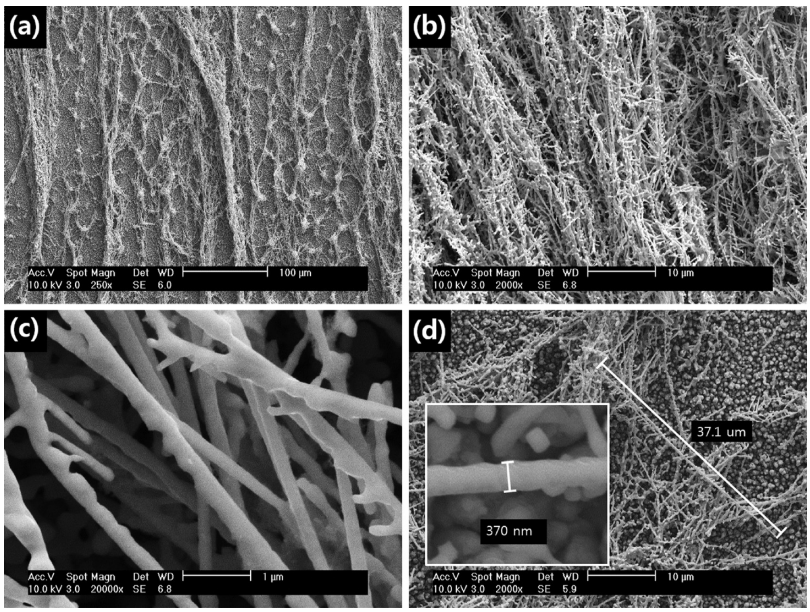

Figure 1. SEM images of the Sn nanofibers that were synthesized by cathodic electrodeposition at −10.5 V for 30 s from an aqueous solution containing 0.25 M $SnSO_4$, 0.7 M H_2SO_4 and 40 g/L Triton X-100.

numerous processes are required to prepare and remove the template, and the growth time is long.[2] Furthermore, because the fabricated nanostructures are easily destroyed and can collapse during the removal of the hard templates, the difficulty in obtaining an intact final product is another serious drawback of template-assisted synthesis. In contrast, template-free synthesis allows for the direct synthesis of single-crystalline 1D nanostructures on the substrate without the use of templates.[20,21] Thus, compared to template-assisted synthesis, this approach offers a strong advantage of a single-step and more cost-effective process. However, because template-free synthesis is based on the crystal anisotropy originating from the crystal structure itself, a limited number of metals have been successfully used to grow 1D nanostructures, which form along one of the crystal axes.[21−23]

In this study, we suggest a novel electrochemical approach for synthesizing single-crystalline 1D Sn nanofibers using an organic compound as a growth modifier. This simple and very effective approach involves the rapid electrochemical deposition of Sn and strong adsorption of the organic compound, Triton X-100 ($(CH_3)_3C-CH_2-C(CH_3)_2-C_6H_6-(OCH_2CH_2)_n-OH$), on a specific crystallographic plane of the Sn electrodeposits. Triton X-100 is a nonionic surfactant composed of a number of hydrophilic oxyethylene groups and a substituted hydrophobic benzene ring.[20] Herein, Triton X-100 plays an important role in the formation of 1D Sn nanofibers because of its suppression of Sn growth along the [100] direction and its promotion of Sn growth in a crystallographic direction normal to the (112) or ($\bar{1}$12) plane. The fabricated electrodeposits exhibit porous structures that are composed of numerous Sn nanofibers arranged in one direction, upward relative to the electrode, with pore volumes existing between the nanofibers. Thus, our approach has several advantages over conventional processes. For example, our process is low-cost, one-step, extremely fast (within a few seconds) and performed at room temperature using a nontoxic bath preparation. Specifically, no additional processes are needed for preparing and removing the templates. Moreover, this process is suitable for mass production on large-area substrates because of the high uniformity of the nanofibers over the entire substrate.

The objective of this work is to investigate the growth mechanism of Sn nanofibers in an electrodeposition process while emphasizing the effects of Triton X-100 on the growth behavior of the Sn nanostructures. In addition, because 1D nanostructures are well suited for use as electrode materials in electrochemical devices, the electrochemical performance of the electrodeposited Sn nanofibers as an anode material for Na-ion batteries was evaluated.

RESULTS AND DISCUSSION

Synthesis and Characterization of Sn Nanofibers by Electrodeposition. Figure 1 shows the morphology of the Sn electrodeposits synthesized by cathodic electrodeposition at −10.5 V for 30 s from an aqueous solution containing 0.25 M $SnSO_4$, 0.7 M H_2SO_4 and 40 g/L Triton X-100. At low magnification (as shown in Figure 1(a)), the surface of the Cu substrate was partly covered with a high density of long electrodeposits. However, the high-magnification SEM images revealed that the electrodeposits were composed of a large number of fine 1D dendritic nanostructures that were interlaced with each other (Figure 1(b) and 1(c)). As depicted in Figure 1(d), a typical synthesized nanowire has an apparent thickness of approximately 370 nm, and the

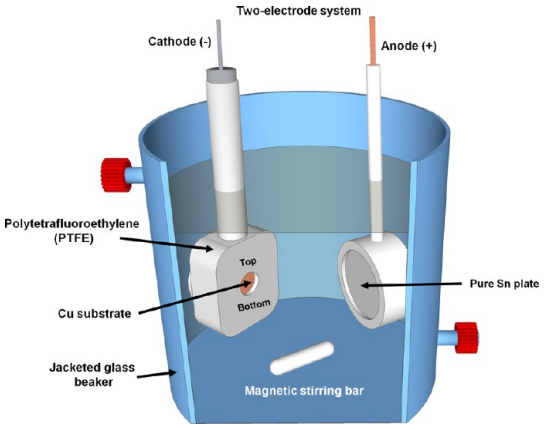

Scheme 1. Schematic illustration of the electrodeposition system for the synthesis of the Sn nanofibers.

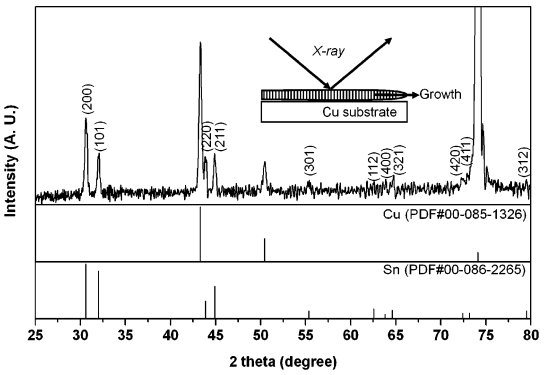

Figure 2. XRD patterns for the Sn nanofibers that were synthesized by cathodic electrodeposition at −10.5 V for 30 s from an aqueous solution containing 0.25 M $SnSO_4$, 0.7 M H_2SO_4 and 40 g/L Triton X-100.

length of the nanofibers was 37.1 μm, which corresponds to an aspect ratio (length-to-width ratio) of approximately 100. Another notable feature in the SEM observations is that the nanofibers were lying parallel to the surface of the substrate and grew in almost the same direction, upward relative to the electrode (from the "bottom" to the "top" of the electrode, as defined in Scheme 1). Because the Sn nanofibers are electrodeposited at a high cathodic potential of −10.5 V, hydrogen gas was generated vigorously (reduction of H^+) that was competitive with Sn electrodeposition (reduction of Sn^{2+}). Herein, the hydrogen bubbles that evolved on the Cu substrate created a continuous path from the substrate to the electrolyte-air interface during the deposition process, which created an electrolyte turbulence near the electrode surface. Therefore, a strong electrolyte current in the upward direction (relative to the electrode) would be induced on the electrode surface, which acts as the driving force for the growth of Sn electrodeposits in the upward direction of the specimen.

The microstructural characteristics of the Sn nanofibers were investigated by XRD analysis. As shown in Figure 2, the XRD pattern verifies the formation of crystalline β-Sn with a tetragonal structure of $I4_1/amd$ and lattice constants of a = 5.832 Å and c = 3.181 Å. However, it is difficult to determine the preferred orientation or the growth direction of the nanofibers from the XRD pattern owing to the absence of a diffraction line with an obviously higher intensity relative to the reference pattern (PDF #00−0865−2265) in the powder diffraction file database (PDF). The diffractometer only collects reflections from the crystallographic planes that are parallel to the substrate, and hence the comparison of the diffraction lines to the reference lines provides information about the crystal orientation of the specimen against the substrate. In this regard, it can be assumed that Bragg diffraction cannot occur for the consecutive crystallographic planes perpendicular to the growth direction when the preferred direction of the crystallites is parallel to the surface of the substrate (*i.e.*, the accurate growth direction of the nanofibers cannot be identified using XRD analysis alone). Indeed, as shown in Figure 1, the axes of most of the electrodeposited Sn nanofibers were parallel to the surface of the Cu substrate. Therefore, the actual growing plane of the nanofiber must not correspond with the preferred orientation observed by the XRD pattern. The inset in Figure 2 schematically shows the difficulties that are inherent in using Bragg diffraction for consecutive crystallographic planes normal to the axis of the Sn nanofibers.

To investigate the growth direction of the Sn nanofibers, further structural analyses were conducted using high-resolution TEM (HRTEM) and selected area electron diffraction (SAED) patterns. As shown in Figure 3, three locations were selected on a Sn nanofiber for observation by HRTEM, the (a) top, (b) bottom and (c) the top of a side branch of the nanofiber. For both (a) and (b), a long-range ordered crystal lattice was observed along the surface of the nanofibers, indicating that the main stem of the nanofiber is a single crystalline. Interestingly, at the middle of the stem, a side branch that inclines away from the axis of the nanofiber at an angle of approximately 29.5° was formed, and the branch shows a long-range ordered crystal lattice in the same direction (Figure 3(c)). The corresponding SAED patterns verified that not only the stem but the side branch of the Sn nanofiber was also composed of a single crystal. The distinctly observed fringe spacing of the nanofibers was 0.291 nm, which was assigned to a d-spacing of 0.29158 nm for the $\{200\}$ set of planes. However, on closer examination it was found that the growth direction of the nanofiber (the axis of the nanofiber) is different from these fringes. This means that the growth direction of the nanofiber is not [100] or [010]. Instead, the SAED patterns reveal that the axis of the Sn nanofiber is identical to a direction normal to the $(\bar{1}12)$ plane. Moreover, the measured angle of 29.5° between the stem and the branch of the nanofiber is well matched with the angle between (112) and $(\bar{1}12)$, which was calculated as 29.48° (Figure 3(d)).

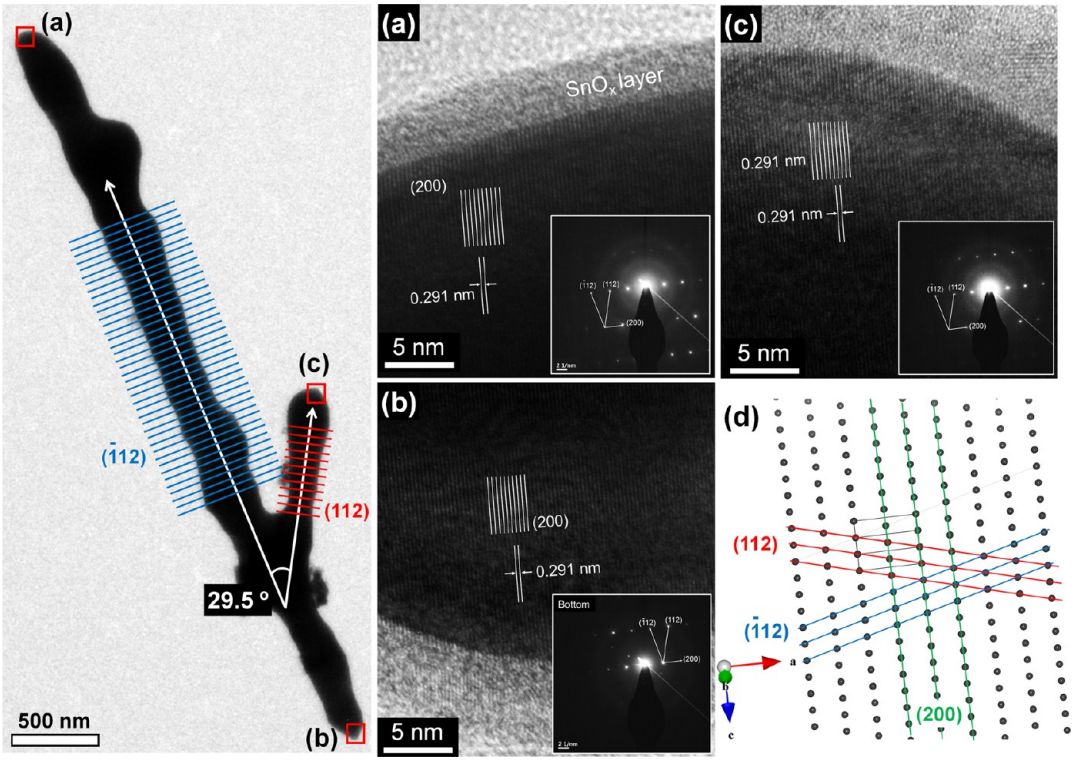

Figure 3. HRTEM images and corresponding selected area electron diffraction (SAED) patterns at the (a) top, (b) bottom and (c) branch of a Sn nanofiber synthesized by cathodic electrodeposition at −10.5 V for 30 s from an aqueous solution containing 0.25 M $SnSO_4$, 0.7 M H_2SO_4 and 40 g/L Triton X-100. (d) The schematic illustration of the {112} and {200} lattice fringes of β-Sn.

Therefore, the HRTEM and SAED patterns suggest that the Sn nanofibers were grown in a direction normal to the (112) or ($\bar{1}$12) plane.

This growth behavior should be noted because β-Sn nanowires are known to preferentially grow along the [100] direction regardless of the synthetic method used.[7,17,19,25−27] In general, crystallographic planes with higher surface free energies are thermodynamically unstable and vulnerable to attack by external atoms.[27] Because the (200) planes of tetragonal β-Sn are the most thermodynamically unstable, anisotropic growth and subsequent predominant growth along the (200) planes are typical characteristics of β-Sn.[26,27] Thus, despite the equivalency of the (100) and (010) planes, most of the 1D Sn nanostructures show [100] directional growth due to this intrinsic crystallographic property of β-Sn.[28] From this viewpoint, the growth of Sn nanofibers along a direction other than the [100] direction is unusual and represents a considerably interesting result.

The largest difference between our synthetic approach and conventional methods is the use of a nonionic surfactant, Triton X-100, which contains both a hydrophilic polyethylene group and a lipophilic hydrocarbon group. Triton X-100 has many applications over a wide range of fields due to its wettability, detergency, superior hard surface, metal-cleaning ability and excellent emulsification performance.[29] In addition, Triton X-100 can function as a suppressor and a brightener in the electrodeposition of Sn/Pd. The addition of Triton X-100 produced a uniform, adherent and semibright deposit by forming a layer of organic molecules on the electrode surface.[30,31] Commonly, adsorbed organic molecules can generally affect the surface diffusion of metal adions or adatoms to stable lattice sites and the deposition kinetics by changing the growth direction of the electrodeposits.[32,33] In this sense, it can be assumed that Triton X-100 suppresses the growth of the Sn crystallites along the [100] direction by adsorption on the (200) plane and promotes the growth of the Sn crystallites in a direction normal to the (112) or ($\bar{1}$12) plane.

The adsorption of Triton X-100 on the (200) plane was confirmed by the electrodeposition of Sn at a relatively low current density of −100 mA/cm^2. As shown in Figure S2 (Supporting Information), the addition of 40 g/L Triton X-100 in the bath results in a significant reduction in the perfection of the [200] crystal orientation in the Sn electrodeposit, whereas the other peaks exhibit no obvious change. In addition, the significant increase in the cathodic overpotential with the addition of Triton X-100 demonstrates that Triton X-100 has a strong suppressive effect on Sn electrodeposition (Figure S3), in agreement with previous studies.[30,31]

According to Zavarine *et al.*,[29] the hydrophobic portion of Triton X-100 maintains adsorption on the electrode surface at all potentials in virtue of the

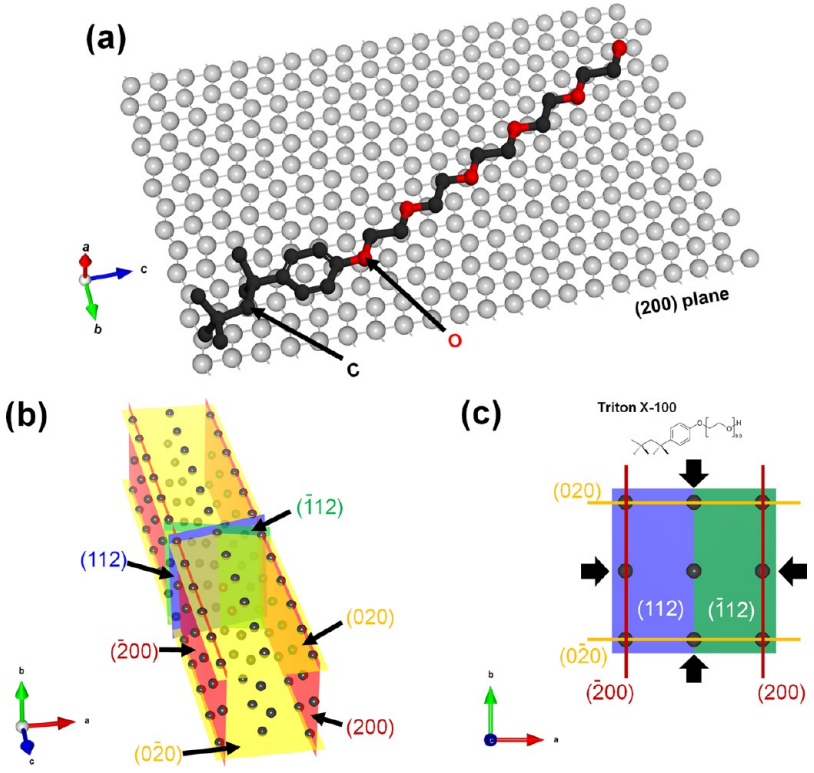

Figure 4. Schematic illustration of (a) the adsorption of Triton X-100 on the (200) plane of β-Sn, (b) the lattice of β-Sn and (c) the corresponding 2D view along the *c*-axis.

overlap of the π-orbitals of the aromatic portions with the localized orbitals of the metal[31] while the strong hydrophilic poly(ethylene oxide) chain stretches into the aqueous phase.[29,34] At higher cathodic potentials, the surface coverage of Triton X-100 is significantly increased by the enhanced metal-to-surfactant interaction (adsorption), causing the poly(ethylene oxide) chain to lie flat on the surface. Under these conditions, Triton X-100 is adsorbed on the electrode surface in an uncoiled but elongated configuration to provide maximum overlap of the unshared p-orbitals of oxygen with the localized metal orbitals.[31] Likewise, because the electrodeposition of Sn in this study was conducted at a high cathodic potential of −10.5 V, the poly(ethylene oxide) chain of Triton X-100 was expected to exhibit strong adsorption on the (200) plane (Figure 4(a)). Although perfect coverage of the surface would be difficult, substantially complete coverage is anticipated for Triton X-100 attributed to its high entropy of the adsorption and the high Triton X-100 concentration in the electrolyte.

Figure 4(b) presents the lattice for the β-Sn phase with lattice constants of a = 5.832 Å and c = 3.181 Å. Because of the equivalency of the (200) and (020) planes of β-Sn, Triton X-100 has suppressive effects on the growth of Sn crystallites along both the [100] and [010] directions. When the surfaces of the (200) and (020) planes are substantially covered with elongated Triton X-100 (Figure 4(c)), the newly reduced Sn atoms from the Sn^{2+} ions in the electrolyte will be forced to attach to the dangling bonds in the (112) and ($\bar{1}$12) planes, which incline away from the (200) plane at angles of 82.56° and 97.44°, respectively. As a result, the crystal growth rates along the *a*- and *b*-axes become much slower than that normal to (112) and ($\bar{1}$12), and hence the Sn electrodeposits spontaneously form 1D nanostructures with a high aspect ratio.

Although the XRD pattern of the nanofiber in Figure 2 suggests that the electrodeposits contain no crystalline phases other than β-Sn, a translucent layer on the surface of the Sn nanofiber with a thickness of approximately 5−7 nm was observed using HRTEM. Figure 5(a) clearly reveals the existence of short-range ordered crystalline lattices along the entire surface of the nanofiber. In addition, the distance between the two adjacent lattice planes was measured as 3.35 Å and was assigned to the {110} planes of tetragonal SnO_2 (a = 4.738 Å, c = 3.187 Å). Furthermore, the high-resolution core-level XPS spectrum of Sn 3d clearly demonstrated that the surface of the Sn nanofiber was covered with two forms of Sn oxide, SnO_2 (~487.71 eV) and SnO (~486.4 eV). As shown in Figure 5(b), the Sn ($3d_{5/2}$) and Sn ($3d_{3/2}$) peaks could be deconvoluted into three peaks each, Sn^{4+} (487.71 and 496.16 eV), Sn^{2+} (486.4 and 494. 75 eV) and Sn^0 (485.58 and 493.95 eV), respectively, which agreed with the values for SnO_2, SnO and metal Sn, respectively.[35,36] Because the peaks centered at 487.71 and 496.16 eV disappeared after 1200 s of ion etching, it was deduced that the inner

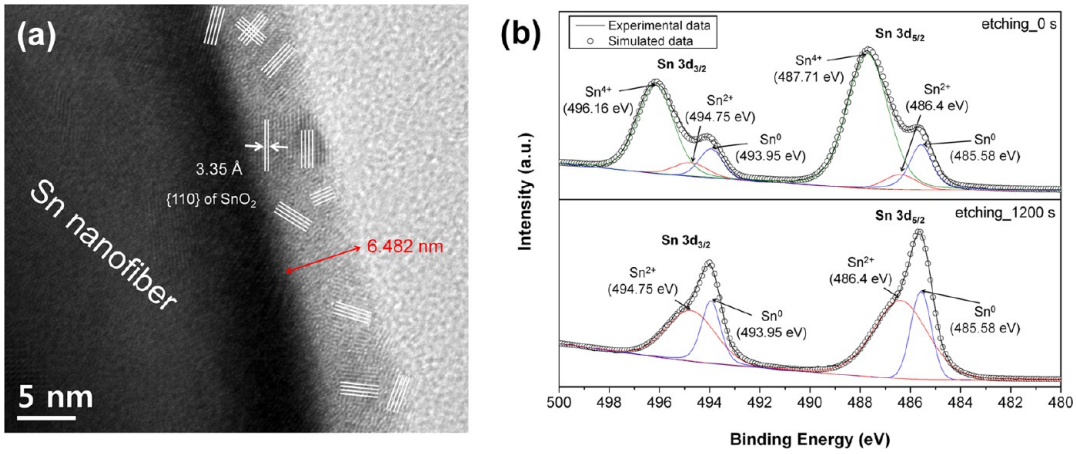

Figure 5. (a) HRTEM image of the surface of the Sn nanofiber and (b) high-resolution XPS spectra for the Sn nanofibers before and after 1200 s of ion etching.

oxide layer was fully composed of amorphous SnO and the outer oxide layer was mainly composed of crystalline SnO_2.

On the basis of these results and the above discussion, a novel growth mechanism for Sn nanofibers in the presence of Triton X-100 is proposed. As illustrated in Scheme 2, at high cathodic potentials, the formation of small nuclei of Sn electrodeposits with dense packing on the surface occurred simultaneously with the vigorous evolution of hydrogen gas (Scheme 2(a)). Herein, the hydrogen bubbles evolving on the Cu substrate diffuse into the electrolyte-air interface, which creates a driving force for the growth of Sn electrodeposits in the upward direction of the specimen. During Sn electrodeposition (under high cathodic potentials), Triton X-100 selectively and strongly adsorbed on the (200) and (020) crystallographic planes of the Sn nuclei (Scheme 2(b)). The adsorption suppressed growth of Sn along the [100] and [010] directions and promoted anisotropic growth of Sn normal to the (112) or ($\bar{1}$12) plane (Scheme 2(c)). Because of the equivalency of the (112) and ($\bar{1}$12) planes in β-Sn, several short side branches that inclined away from the axis of the main stem at 29.48° were formed on the main stem of the nanofiber (Scheme 2(d)).

Electrochemical Properties of the Sn Nanofibers for Na-Ion Batteries. Recently, rechargeable Na-ion batteries have received considerable attention as a near-term alternative to Li-ion batteries for large-scale systems, such as grid storage devices, because of low cost, relatively low redox potential (0.3 V higher than that of Li/Li^+) and the high natural abundance of Na.[37−39] Accordingly, extensive studies have been conducted to find suitable electrode materials with a high specific capacity, low irreversible loss, high Coulombic efficiency and long cycle life. Among the various candidates, Sn is one of the most attractive anode materials due to its high theoretical capacity and low reaction potential.[24,40−48] When assuming complete sodiation of Sn into $Na_{15}Sn_4$, the capacity of Sn is approximately 847 mAh g^{-1},[46] which is substantially greater than the reversible capacity of hard carbon (as high as 300 mAh g^{-1}).[49,50] However, pure Sn electrodes exhibit poor cyclability on account of the structural failure of Sn that results from a significant volume change (up to approximately 420%) during sodiation/desodiation.[24] Consequently, major challenges remain for improving the cycle stability of the Sn electrodes. One possible strategy for overcoming such a problem is to make a nanostructured or nanoscale electrode for facilitating the relaxation of material stress. Indeed, according to Yang *et al.*,[51] decreased particle size can increase the cycling stabilities of Sn electrodes for Li-ion batteries. Li−Sn alloys with particle diameters ranging from 200−400 nm exhibited less cracking and pulverization than alloys with larger, micron-sized particles, demonstrating that the cycling performance of Li-alloy anodes is highly dependent on the morphology of the metallic matrix. Because the volume expansion of Sn upon sodiation is similar to that upon lithiation,[24,52] considerable improvements in cycle performance may be expected for nanocrystalline Sn anodes. From this perspective, the Sn nanofibers fabricated in this study may provide an ideal solution to problems involving the use of pure Sn in Na-ion batteries.

The cycle performance and Coulombic efficiency of the Sn nanofibers were investigated at a rate of 0.1 C (based on the mass of Sn) over a voltage range of 0.001 to 0.65 V (*vs* Na/Na^+). On the basis of the half-cell reaction in this study, the insertion of Na^+ into the Sn nanofiber electrode is referred to as discharge, and the extraction of Na^+ from the electrode is referred to as charge. As shown in Figure 6(a), the Sn nanofibers exhibit a high reversible capacity and excellent cycle performance. Specifically, the charge capacity was maintained at 776.26 mAh g^{-1} after 100 cycles, which corresponded to 95.09% of the initial charge capacity

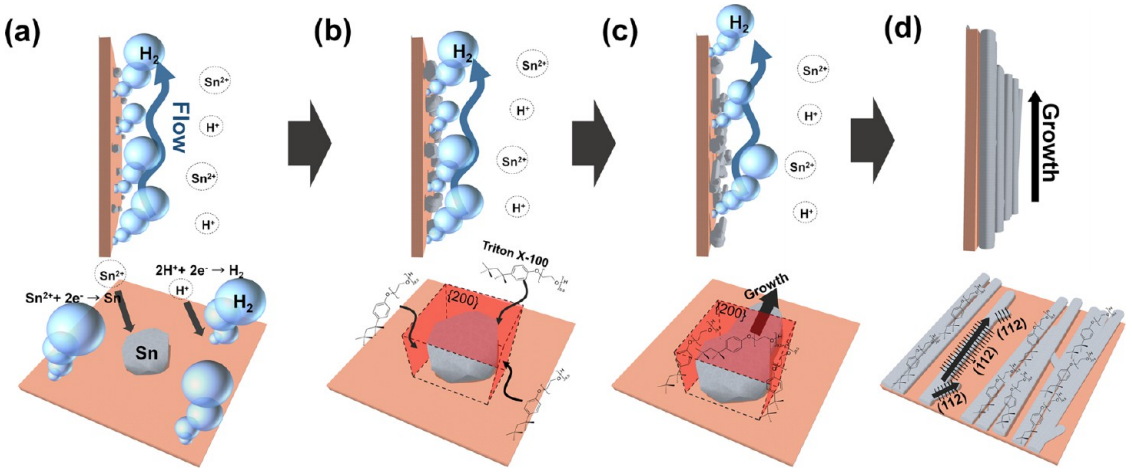

Scheme 2. Simplified description of the growth mechanism of the Sn nanofibers by cathodic electrodeposition. Hydrogen bubbles that evolved on the substrate create a strong electrolyte current from the bottom to the top of the electrode. This process acts as the driving force for the growth of Sn electrodeposits in the upward direction of the specimen. The (200) planes are privileged sites for the adsorption of Triton X-100, and consequently, the Sn nanofibers grow along a direction normal to the (112) or ($\bar{1}$12) plane.

(816.37 mAh g^{-1}). Although the first- and second-cycle Coulombic efficiencies were only 68.03 and 90.96%, respectively, the efficiency steadily increased to 98.27% by the 100th cycle. The high aspect ratio of the Sn nanofibers provides a high reversible capacity by increasing the surface-to-volume ratio and reducing the Na diffusion distances. However, the extremely large surface areas of these nanofibers may result in significant electrolyte decomposition problems. Generally, low Coulombic efficiency is mainly attributed to the irreversible Coulombic losses caused by electrolyte decomposition, which occurs constantly on the surface of Sn.[40,53] This irreversible consumption occurs because the electrolyte is not completely optimized for Na-ion batteries. In this experiment, we used fluoroethylene carbonate (FEC) as an electrolyte additive, which has been reported to inhibit electrolyte decomposition by modifying the surface passivation layer.[53] However, the extensive decomposition of the electrolyte was not sufficiently suppressed due to the large surface area. Despite the low Coulombic efficiency, the excellent retention of the charge capacity indicated that the Sn nanofibers reversibly reacted with Na with a high stability and that abrupt capacity deterioration due to the detachment of Sn was completely suppressed, unlike in the case of a typical pure Sn electrode.[24]

The rate capabilities of the Sn nanofibers with varying C rates are shown in Figure 6(b). The Sn nanofibers exhibit a charge capacity of 808.19 mAh g^{-1} at a rate of 0.1 C and retain a high reversible capacity of 784.53 mAh g^{-1} at 1 C (only a 2.93% reduction). Although the charge capacity decreased sharply from 2 to 5 C, the initial capacity (790 mAh g^{-1} at the 40th cycle) was completely restored with good cycle stability when the current density returned to 0.1 C from 5 C in the 36th cycle. The recovery of the capacity demonstrates that the structure of the Sn nanofibers is sustained, even at high C rates, and implies that the rapid reduction in the capacity at a C rate of 2 may be attributed to the imperfect desodiation of Na_xSn. Despite the low discharging capacity at a C rate of 0.1, increasing overpotentials resulted from the slow diffusion of Na^+ ions in the bulk material, which resulted in unfinished desodiation reactions at a cutoff voltage of 0.65 V. Thus, the reversible capacity decreased dramatically as the charging current densities increased (as shown in Figure 6(b)).

Another notable feature of the electrochemical properties of the Sn nanofibers is a gradual change in the charge profiles from the first to fourth cycle. This behavior implies that the electrochemical reactions of the Sn nanofibers take a different reaction pathway upon cycling. As shown in Figure 6(c), the first charge curve for the Sn nanofibers has three distinct plateaus, denoted as I, II and III in order of increasing Na content. On the basis of the results of the previous study,[24] it can be suggested that the electrochemical sodiation/desodiation of the Sn nanofibers undergoes the following reactions in the voltage range of 0.001 to 0.650 V.

$$\text{Plateau I}: \text{Na} + (\text{NaSn}_x + \beta\text{-Sn}) \leftrightarrow \alpha\text{-NaSn (amorphous)}$$

$$\text{Plateau II}: 5\text{Na} + 4(\alpha\text{-NaSn}) \leftrightarrow \text{Na}_9\text{Sn}_4 \text{ (crystalline)}$$

$$\text{Plateau III}: 6\text{Na} + \text{Na}_9\text{Sn}_4 \leftrightarrow \text{Na}_{15}\text{Sn}_4 \text{ (crystalline)}$$

However, in the subsequent cycles, the plateaus at 0.17 V (plateau III) and 0.27 V (plateau II) gradually merge into a single plateau at 0.2 V (plateau IV) whereas the plateau at 0.55 (plateau I) did not change.

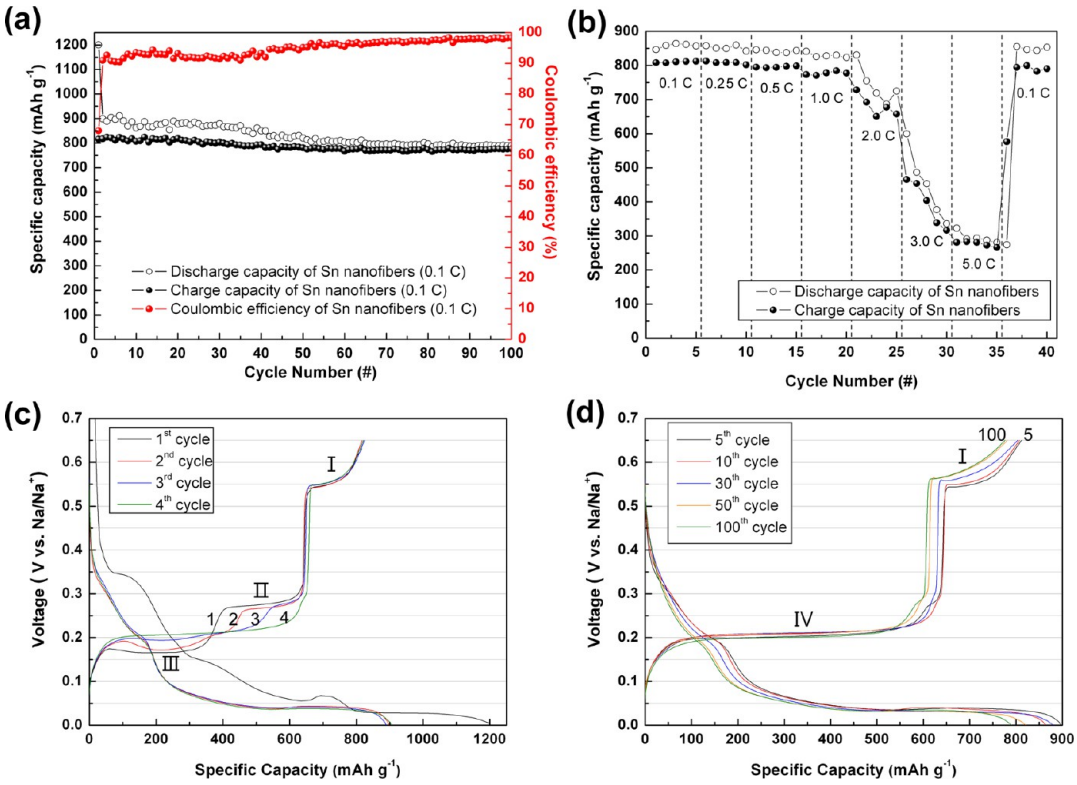

Figure 6. (a) Cycle performance and Coulombic efficiency of the Sn nanofibers at a rate of 0.1 C over a voltage range of 0.001 to 0.65 V (*vs* Na/Na^+). (b) Specific capacities of the Sn nanofibers with the current density varying from 0.1 to 5 C and back to 0.1 C between 0.001 and 0.65 V with a fixed discharging current density of 0.1 C. Charge–discharge curves of the Sn nanofibers at (c) the 1st, 2nd, 3rd and 4th cycles and (d) the 5th, 10th, 30th and 100th cycles.

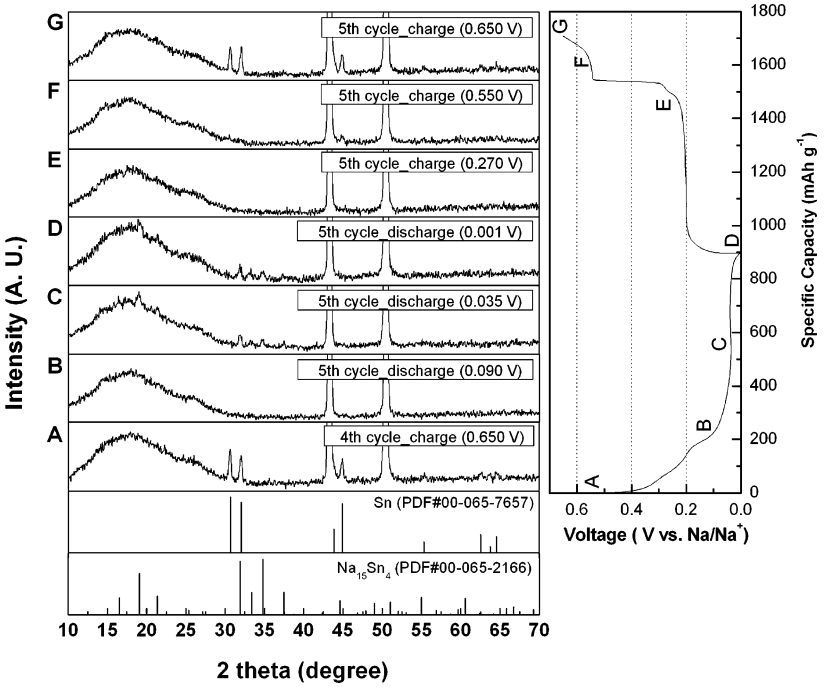

Figure 7. XRD patterns for the Sn nanofibers at various stages during the 5th cycle.

The merging of the two plateaus into a single plateau occurs during the second and third cycles and is complete at the fourth cycle. This profile change suggests that the desodiation reaction can proceed directly from $Na_{15}Sn_4$ to α-NaSn (amorphous) without forming the Na_9Sn_4 intermediate. In fact, the phase

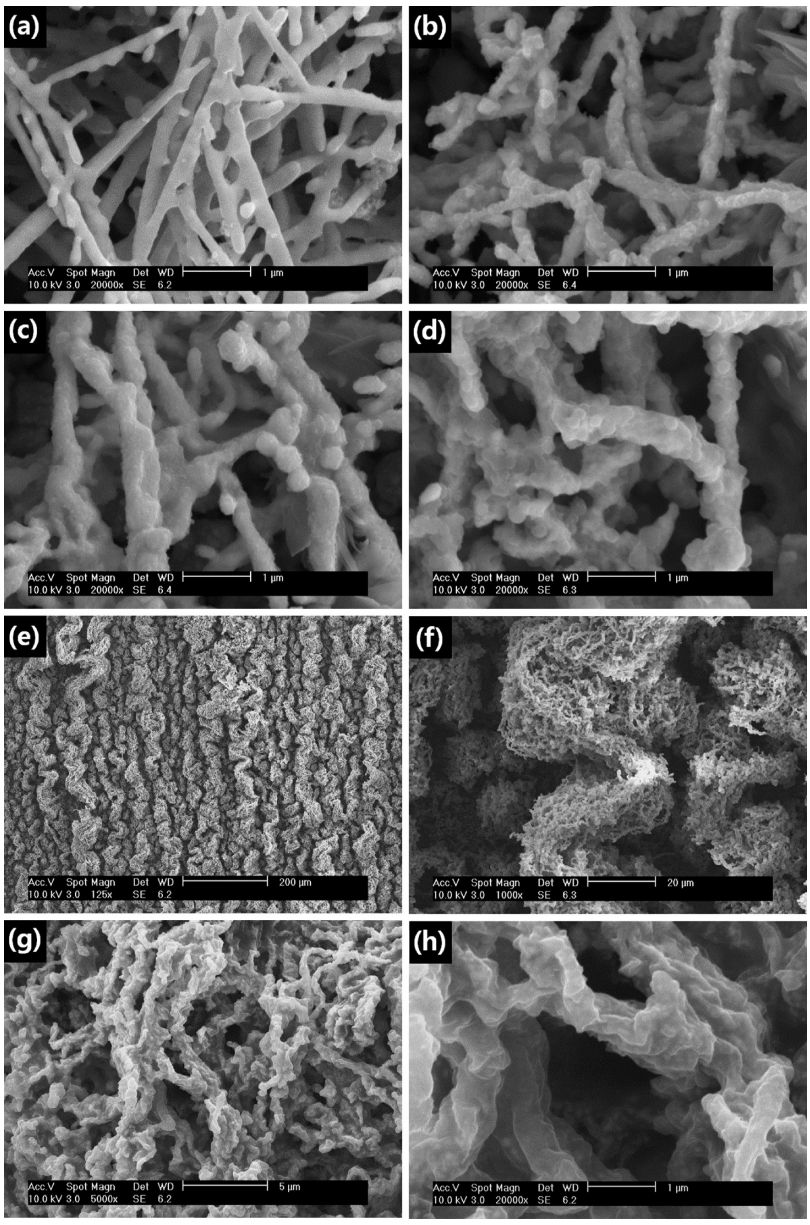

Figure 8. SEM images of the Sn nanofibers (a) as deposited, (b) after 1 cycle, (c) after 2 cycles, (d) after 3 cycles and (e−h) after 100 cycles.

formed between plateaus II and III is controversial because the XRD pattern for this phase does not correspond to the pattern reported for the crystalline Na_9Sn_4 phase.[24,41] According to Ellis *et al.*,[41] the inability of Sn and Na atoms to arrange into complex structures, such as Na_9Sn_4, at room temperature may account for the formation of the metastable phase instead of the expected thermodynamically stable phase. Consequently, the formation of the metastable phase of Na_9Sn_4 was avoided, and $Na_{15}Sn_4$ was directly converted into the amorphous phase of NaSn (IV) after the fifth cycle. The voltage profiles of the Sn nanofibers exhibited the same behavior between the fifth to the 100th cycles (Figure 6(d)), indicating that highly stable sodiation/desodiation reactions for the Sn nanofiber (IV ↔ I) occur repeatedly without changes in the reaction pathway.

$$\text{Plateau IV}: 11\text{Na} + 4(\alpha\text{-NaSn}) \leftrightarrow \text{Na}_{15}\text{Sn}_4 \text{ (crystalline)}$$

To confirm the proposed electrochemical reactions of the Sn nanofibers with Na, the phase changes of Sn during cycling were investigated using *ex situ* XRD. The sodiated Na−Sn alloy phases were examined at the middle or end of the plateaus. Figure 7 shows the XRD patterns for the electrode when discharged to A, B, C, and D or when charged to E, F, G and H during the fifth cycle, as marked in the voltage profile. Although the diffraction peaks of crystalline β-Sn were obtained at 0.65 V after 4 cycles (A), the initial Na−Sn alloy phase at 0.65 V did not consist of β-Sn solely, but was composed

of crystalline β-Sn and an amorphous Na-poor Sn alloy phase. This result occurred because full desodiation of the Na−Sn alloy is impossible at a voltage range of between 0.001 and 0.65 V.[24] At the end of the initial discharge plateau (B), the diffraction peaks of β-Sn completely vanished, and no peaks were observed. This finding indicated that β-Sn was completely converted to an amorphous Na−Sn phase. Crystalline $Na_{15}Sn_4$ was formed instead of the metastable crystalline phase in the middle of the following plateau (C), which demonstrates that the metastable Na_9Sn_4 was not formed during the fifth discharge. When completely sodiated (D), the phase structure of the $Na_{15}Sn_4$ phase was maintained. In the following charging process, the $Na_{15}Sn_4$ phase disappeared at 0.270 V during charging (E), and the diffraction peaks corresponding to β-Sn reappeared at 0.650 V (G). The XRD analysis verifies that the sodiation process (A → D) and the desodiation process (D → G) occurred reversibly and that the Sn nanofibers undergo two phase transitions during sodiation or desodiation.

To investigate the structural stability of the Sn nanofibers, the morphology of the electrode after cycling was characterized by *ex situ* SEM. As shown in Figure 8(b), after 1 cycle, the nanofiber morphology was slightly distorted from the initial straight morphology (Figure 8(a)). However, the apparent dimensions of the nanofibers did not greatly change despite the severe volumetric changes. While the nanofiber diameter appeared to increase after 2 and 3 cycles, the 1D morphology of the nanofibers was maintained (Figure 8(c) and 8(d)), indicating that the Sn nanofibers undergo nearly reversible volumetric expansion and shrinkage during sodiation/desodiation. Even after 100 cycles, no obvious cracks or fractures were formed on the nanofibers (Figure 8(g) and Figure 8(h)). In particular, the nanofibers sustained the 1D morphology and good electrical contact with the current collector without any loss of the active materials (Figure 8(e) and Figure 8(f)). Therefore, the superior mechanical stability of the Sn nanofibers is considered as a major contributor to the excellent cycle stability shown in Figure 7(a).

Considering the large volume changes (up to approximately 420%), the nanofibers may undergo highly anisotropic expansion during sodiation/desodiation to account for the maintenance of the 1D morphology over cycling. Because the outer free surfaces induce greater expansion in the radial direction and lesser expansion in the axial direction, greater expansion in the radial direction of the Sn nanofiber during sodiation is more favorable than that in the other directions in the bulk.[54] In general, the particle-like structure deposited on the substrate may be vulnerable to the stress accompanying the volume changes. This is because the 0-dimensional particles would expand in all directions except downward during sodiation but contract in all directions during desodiation.[24] Thus, compared to 0D micron-sized particles and 2D layered structures, the high aspect ratio of 1D nanostructured Sn can better accommodate sodiation-induced stress and effectively suppress the mechanical degradation of the material, such as pulverization or fracturing.

CONCLUSIONS

In this study, Sn nanofibers with a high aspect ratio were successfully synthesized using a simple electrodeposition process from an aqueous solution without templates. This approach involves the rapid electrochemical deposition of Sn and the strong adsorption of Triton X-100 on the {200} crystallographic planes of the Sn crystallites, which induce anisotropic growth of 1D Sn nanofibers normal to the (112) or ($\bar{1}$12) plane. As electrode materials for Na-ion batteries, the Sn nanofibers exhibited a high reversible capacity and excellent cycle performance. The charge capacity was maintained at 776.26 mAh g^{-1} after 100 cycles, which corresponds to a 95.09% retention of the initial charge capacity. The superior electrochemical performance of the Sn nanofibers was mainly attributed to their high mechanical stability to sodiation, which originates from their highly anisotropic expansion and the pore volumes existing between the nanofibers. Although further research is required to improve the Coulombic efficiency and rate capability, the Sn nanofibers synthesized by this simple electrodeposition process demonstrate the feasibility of using binder- and conductive-agent-free Sn as a high-performance anode material in advanced Na-ion batteries. Furthermore, the synthetic approach suggested in this study provides a facile template-free and cost-effective process for fabricating 1D nanostructures, and this methodology can be readily applied across a variety of electrochemistry and nanotechnology fields.

EXPERIMENTAL SECTION

Sn nanofibers were synthesized by potentiostatic electrodeposition at −10.5 V for 30 s from an aqueous solution containing 0.25 M $SnSO_4$, 0.7 M H_2SO_4 and 40 g/L Triton X-100. The electrodeposition was conducted using a two-electrode cell, with nodular Cu foil as the cathode (Figure S1) and a pure Sn plate as the anode. The distance between the cathode and the anode was 1.5 cm, and the solution was magnetically stirred at 180 rpm. The electrodeposition system for the fabrication of Sn nanofibers is schematically illustrated in Scheme 1. All experiments were conducted at room temperature (20 ± 0.5 °C). The fabricated Sn nanofibers were dried in a vacuum for 12 h after rinsing with distilled water to prevent further Sn oxidation. The deposition mass was measured from the difference of mass before and after the Sn electrodeposition, and the average mass of deposited Sn was measured to be approximately 0.34 mg.

The surface morphology and the dimensions of the electrodeposits were examined by scanning electron microscopy (SEM). The crystal structures of the electrodeposits were

investigated using X-ray diffraction (XRD) and high-resolution transmission electron microscopy (HRTEM). To prepare the specimens for TEM, the dried Sn nanofibers were scraped from the substrates and dispersed in ethanol *via* sonication for 1 h. X-ray photoelectron spectroscopy (XPS) was used to characterize the surface of the Sn nanofibers.

The electrochemical properties of the Sn nanofibers were investigated using Swagelok-type cells that were assembled in an Ar-filled glovebox. Each cell consisted of a Sn electrode sheet (with an area of 1 cm^2) and a Na metal film (with an area of 1 cm^2) without a separator.[24] The electrolyte was anhydrous propylene carbonate (PC) with 1 M $NaClO_4$ and 2 vol % fluoroethylene carbonate (FEC). The charge/discharge characteristics of the electrode were examined galvanostatically at a current density of 84.7 mA g^{-1} (0.1 C rate) and between 0.001 and 0.65 V (*vs* Na/Na^+). The rate capabilities of the electrode were evaluated at different current densities over voltage ranges of between 0.001 and 0.65 V (*vs* Na/Na^+). To examine the morphology and phase structure changes of the electrodes with cycling, *ex situ* SEM observation and XRD analyses were performed on each electrode. For *ex situ* SEM characterization, the cycled electrodes were extracted from the Swagelok-type cells and rinsed with anhydrous dimethyl carbonate (DMC). In addition, for the *ex situ* XRD analysis, the cycled samples were sealed with Kapton tape in an Ar-filled glovebox.

Conflict of Interest: The authors declare no competing financial interest.

Acknowledgment. This work was supported by the Center for Inorganic Photovoltaic Materials (No. 2013-001796) grant funded by the Korea Government (MSIP) and Basic Science Research Program through the National Research Foundation of Korea (NRF) funded by the Ministry of Education, Science and Technology (Project No. NRF-2010-0024752).

Supporting Information Available: The morphology of a nodular Cu foil, XRD patterns for Sn electrodeposits at a constant current density of −100 mA/cm^2, the potentiodynamic polarization curve of Sn electrodeposition, electrochemical properties of Sn nanofibers without FEC and differential capacity plots of Sn nanofibers. This material is available free of charge *via* the Internet at http://pubs.acs.org.

REFERENCES AND NOTES

1. Lieber, C. M. One-Dimensional Nanostructures: Chemistry, Physics & Applications. *Solid State Commun.* **1998**, *107*, 607–616.
2. Xia, Y.; Yang, P.; Sun, Y.; Wu, Y.; Mayers, B.; Gates, B.; Yin, Y.; Kim, F.; Yan, H. One-Dimensional Nanostructures: Synthesis, Characterization, and Applications. *Adv. Mater.* **2003**, *15*, 353–389.
3. Zhai, T.; Fang, X.; Li, L.; Bando, Y.; Golberg, D. One-Dimensional Cds Nanostructures: Synthesis, Properties and Applications. *Nanoscale* **2010**, *2*, 168–187.
4. Koenigsmann, C.; Wong, S. S. One-Dimensional Noble Metal Electrocatalysts: A Promising Structural Paradigm for Direct Methanol Fuel Cells. *Energy Environ. Sci.* **2011**, *4*, 1161–1176.
5. Hicks, L. D.; Dresselhaus, M. S. Thermoelectric Figure of Merit of A One-Dimensional Conductor. *Phys. Rev. B: Condens. Matter Mater. Phys.* **1993**, *47*, 16631–16634.
6. Sun, C. Q. The Lattice Contraction of Nanometre-Sized Sn and Bi Particles Produced by An Electrohydrodynamic Technique. *J. Phys.: Condens. Matter* **1999**, *11*, 4801–4803.
7. Tian, M.; Wang, J.; Snyder, J.; Kurtz, J.; Liu, Y.; Schiffer, P.; Mallouk, T. E.; Chan, M. H. W. Synthesis and Characterization of Superconducting Single-Crystal Sn Nanowires. *Appl. Phys. Lett.* **2003**, *83*, 1620–1622.
8. Wu, Y.; Xiang, J.; Yang, C.; Lu, W.; Lieber, C. M. Single-Crystal Metallic Nanowires and Metal/Semiconductor Nanowire Heterostructures. *Nature* **2003**, *430*, 61–65.
9. Shen, G. Z.; Chen, D. One-Dimensional Nanostructures for Electronic and Optoelectronic Devices. *Front. Optoelectron. China* **2010**, *3*, 125–138.
10. Zhuang, S.; Xu, X.; Pang, Y.; Hu, J.; Yang, C.; Tong, L.; Zhou, Y. PEGME-Bonded SnO_2 Quantum Dots for Excellent Photocatalytic Activity. *RSC Adv.* **2013**, *3*, 20422–20428.
11. Kolmakov, A.; Zhang, Y.; Cheng, G.; Moskovits, M. Detection of CO and O_2 using Tin Oxide Nanowire Sensors. *Adv. Mater.* **2003**, *15*, 997–1000.
12. Kuang, Q.; Lao, C.; Zhong, L. W.; Xie, Z.; Zheng, L. High-Sensitivity Humidity Sensor Based on A Single SnO_2 Nanowire. *J. Am. Chem. Soc.* **2007**, *129*, 6070–6071.
13. Choi, N.-S.; Yao, Y.; Cui, Y.; Cho, J. One Dimensional Si/Sn-Based Nanowires and Nanotubes for Lithium-Ion Energy Storage Materials. *J. Mater. Chem.* **2011**, *21*, 9825–9840.
14. Han, Y.; Wu, X.; Ma, Y.; Gong, L.; Qu, F.; Fan, H. Porous SnO_2 Nanowire Bundles for Photocatalyst and Li Ion Battery Applications. *CrystEngComm* **2011**, *13*, 3506–3510.
15. Wang, J.-G.; Tian, M.-L.; Kumar, N.; Mallouk, T. E. Controllable Template Synthesis of Superconducting Zn Nanowires with Different Microstructures by Electrochemical Deposition. *Nano Lett.* **2005**, *5*, 1247–1253.
16. Cao, H.; Xu, Y.; Hong, J.; Liu, H.; Yin, G.; Li, B.; Tie, C.; Xu, Z. Sol-gel Template Synthesis of An Array of Single Crystal CdS Nanowires on A Porous Alumina Template. *Adv. Mater.* **2001**, *13*, 1393–1394.
17. Shin, H. S.; Yu, J. Size-Dependent Thermal Instability and Melting Behavior of Sn Nanowires. *Appl. Phys. Lett.* **2007**, *91*, 173106.
18. Liu, H.; Ye, Z.; Zhang, H.; Wu, W.; Luo, Z.; Rathnayaka, K. D. D.; Naugle, D. G. Superconducting Proximity Effect in Single-Crystal Sn Nanowires. *Phys. B* **2008**, *403*, 1542–1543.
19. Shin, H. S.; Yu, J.; Song, J. Y.; Park, H. M. Size Dependence of Lattice Deformation Induced by Growth Stress in Sn nanowires. *Appl. Phys. Lett.* **2009**, *94*, 011906.
20. Rinne, C. L.; Hren, J. J.; Fedkiw, P. S. Electrodeposition of Tin Needle-Like Structures. *J. Electrochem. Soc.* **2002**, *149*, C150–C158.
21. Mackay, D. T.; AJanish, M. T.; Sahaym, U.; Kotula, P. G.; Jungjohann, K. L.; Carter, C. B.; Norton, M. G. Template-Free Electrochemical Synthesis of Tin Nanostructures. *J. Mater. Sci.* **2014**, *49*, 1476–1483.
22. She, G.-W.; Zhang, X.-H.; Shi, W.-S.; Fan, X.; Chang, J. C.; Lee, C.-S.; Lee, S.-T.; Liu, C.-H. Controlled Synthesis of Oriented Single-Crystal ZnO Nanotube Arrays on Transparent Conductive Substrates. *Appl. Phys. Lett.* **2008**, *92*, 053111.
23. She, G.; Shi, W.; Zhang, X.; Wong, T.; Cai, Y.; Wang, N. Template-Free Electrodeposition of One-Dimensional Nanostructures of Tellurium. *Cryst. Growth Des.* **2009**, *9*, 663–666.
24. Nam, D.-H.; Hong, K.-S.; Lim, S.-J.; Kim, T.-H.; Kwon, H.-S. Electrochemical Properties of Electrodeposited Sn Anodes for Na-Ion Batteries. *J. Phys. Chem. C* **2014**, *118*, 20086–20093.
25. Tian, M.; Wang, J.; Kurtz, J. S.; Liu, Y.; Chan, M. H. W.; Mayer, T. S.; Mallouk, T. E. Dissipation in Quasi-One-Dimensional Superconducting Single-Crystal Sn Nanowires. *Phys. Rev. B: Condens. Matter Mater. Phys.* **2005**, *71*, 104521.
26. Hsu, Y.-J.; Lu, S.-Y. Growth Mechanism and Superconductivity. *J. Phys. Chem. B* **2005**, *109*, 4398–4403.
27. Hsu, Y.-J.; Lu, S.-Y.; Lin, Y.-F. Nanostructures of Sn and Their Enhanced, Shape-Dependent Superconducting Properties. *Small* **2006**, *2*, 268–273.
28. Kim, Y.-S.; Lee, S. M.; Song, J. Y. Surface-Stress-Induced Elongation of β-Sn Metal Nanowires: A Density-Functional Study. *Appl. Surf. Sci.* **2010**, *256*, 3603–3606.
29. Zavarine, I. S.; Khaselev, O.; Zhang, Y. Spectroelectrochemical Study of The Effect of Organic Additives on The Electrodeposition of Tin. *J. Electrochem. Soc.* **2003**, *150*, C202–C207.
30. Kohl, P. A. The High Speed Electrodeposition of Sn/Pb Alloys. *J. Electrochem. Soc.* **1982**, *129*, 1196–1201.
31. Meibuhr, S.; Yeager, E.; Kozawa, A.; Hovorka, F. The Electrochemistry of Tin I. Effects of Nonionic Addition Agents on Electrodeposition from Stannous Sulfate Solutions. *J. Electrochem. Soc.* **1963**, *110*, 190–202.
32. Nam, D.-H.; Kim, R.-H.; Han, D.-W.; Kim, J.-H.; Kwon, H.-S. Effects of $(NH_4)_2SO_4$ and BTA on The Nanostructure of

Copper Foam Prepared by Electrodeposition. *Electrochim. Acta* **2011**, *56*, 9397–9405.
33. Nam, D.-H.; Hong, K.-S.; Kim, J.-S.; Lee, J.-L.; Kim, G.-E.; Kwon, H.-S. Synergistic Effects of Coumarin and cis-2-Butene-1,4-Diol on High Speed Electrodeposition of Nickel. *Surf. Coat. Technol.* **2014**, *248*, 30–37.
34. Fang, M.; Huang, T.; Gu, T. Surface Enhanced Raman Scattering of Surfactants Adsorbed on Silver Mirror Surfaces. *Spectrochim. Acta* **1993**, *49A*, 1009–1013.
35. Li, P. G.; Guo, X.; Wang, X. F.; Tang, W. H. Photoluminescence and Dielectric Properties of O-Deficient SnO_2 Nanowires. *J. Alloys Compd.* **2009**, *479*, 74–77.
36. Lu, F.; Ji, X.; Yang, Y.; Deng, W.; Banks, C. E. Room Temperature Ionic Liquid Assisted Well-Dispersed Core-Shell Tin Nanoparticles Through Cathodic Corrosion. *RSC Adv.* **2013**, *3*, 18791–18793.
37. Ong, S.; Chevrier, V.; Hautier, G.; Jain, A.; Moore, C.; Kim, S.; Ma, X.; Ceder, G. Voltage, Stability and Diffusion Barrier Differences Between Sodium-Ion and Lithium-Ion Intercalation Materials. *Energy Environ. Sci.* **2011**, *4*, 3680–3688.
38. Nam, D.-H.; Hong, K.-S.; Lim, S.-J.; Kwon, H.-S. Electrochemical Synthesis of A Three-Dimensional Porous Sb/Cu_2Sb Anode for Na-ion Batteries. *J. Power Sources* **2014**, *247*, 423–427.
39. Farbod, B.; Cui, K.; Kalisvaart, W. P.; Kupsta, M.; Zahiri, B.; Kohandehghan, A.; Lotfabad, E. M.; Li, Z.; Luber, E. J.; Mitlin, D. Anodes for Sodium Ion Batteries Based on Tin-Germanium-Antimony Alloys. *ACS Nano* **2014**, *8*, 4415–4429.
40. Baggetto, L.; Allcorn, E.; Manthiram, A.; Veith, G. M. Cu_2Sb Thin Films as Anode for Na-ion Batteries. *Electrochem. Commun.* **2013**, *27*, 168–171.
41. Ellis, L. D.; Hatchard, T. D.; Obrovac, M. N. Reversible Insertion of Sodium in Tin. *J. Electrochem. Soc.* **2012**, *159*, A1801–A1805.
42. Datta, M. K.; Eur, R.; Saha, P.; Kadakia, K.; Park, S. K.; Kumta, P. N. Tin and Graphite Based Nanocomposites: Potential Anode for Sodium Ion Batteries. *J. Power Sources* **2013**, *225*, 316–322.
43. Wang, J. W.; Liu, X. H.; Mao, S. X.; Huang, J. Y. Microstructural Evolution of Tin Nanoparticles during *In Situ* Sodium Insertion and Extraction. *Nano Lett.* **2012**, *12*, 5897–5902.
44. Komaba, S.; Matsuura, Y.; Ishikawa, T.; Yabuuchi, N.; Murata, W.; Kuze, S. Redox Reaction of Sn-Polyacrylate Electrodes in Aprotic Na Cell. *Electrochem. Commun.* **2012**, *21*, 65–68.
45. Baggetto, L.; Ganesh, P.; Meisner, R. P.; Unocic, R. R.; Jumas, J.-C.; Bridges, C. A.; Veith, G. M. Characterization of Sodium Ion Electrochemical Reaction with Tin Anodes: Experiment and Theory. *J. Power Sources* **2013**, *234*, 48–59.
46. Chevrier, V. L.; Ceder, G. Challenges for Na-Ion Negative Electrodes. *J. Electrochem. Soc.* **2011**, *158*, A1011–A1014.
47. Zhu, H.; Jia, Z.; Chen, Y.; Weadock, N.; Wan, J.; Vaaland, O.; Han, X.; Li, T.; Hu, L. Tin Anode for Sodium-Ion Batteries Using Natural Wood Fiber as A Mechanical Buffer and Electrolyte Reservoir. *Nano Lett.* **2013**, *13*, 3093–3100.
48. Liu, Y.; Xu, Y.; Zhu, Y.; Culver, J. N.; Lundgren, C. A.; Xu, K.; Wang, C. Tin-Coated Viral Nanoforests as Sodium-Ion Batteries. *ACS Nano* **2013**, *7*, 3627–3634.
49. Stevens, D. A.; Dahn, J. R. High Capacity Anode Materials for Rechargeable Sodium-Ion Batteries. *J. Electrochem. Soc.* **2000**, *147*, 1271–1273.
50. Xia, X.; Dahn, J. R. Study of The Reactivity of Na/Hard Carbon with Different Solvents and Electrolytes. *J. Electrochem. Soc.* **2012**, *159*, A515–A519.
51. Yang, J.; Winter, M.; Besenhard Small Particle Size Multiphase Li-Alloy Anodes for Lithium-Ion-Batteries, J.O. *Solid State Ionics* **1996**, *90*, 281–287.
52. Nam, D. H.; Kim, R. H.; Lee, C. L.; Kwon, H. S. Highly Reverisible Sn-Co Alloy Anode Using Porous Cu Foam Substrate for Li-Ion Batteries. *J. Electrochem. Soc.* **2012**, *159*, A1822–A1826.
53. Komaba, S.; Ishikawa, T.; Yabuuch, N.; Murata, W.; Ito, A.; Ohsawa, Y. Fluorinated Ethylene Carbonate as Electrolyte Additive for Rechargeable Na Batteries. *ACS Appl. Mater. Interfaces* **2011**, *3*, 4165–4168.
54. Song, T.; Xia, J.; Lee, J.-H.; Lee, D. H.; Kwon, M.-S.; Choi, J.-M.; Wu, J.; Doo, S. K.; Chang, H.; Park, W. I.; *et al.* Arrays of Sealed Silicon Nanotubes as Anodes for Lithium Ion Batteries. *Nano Lett.* **2010**, *10*, 1710–1716.